Influence of macroscopic interface curvature on dendritic patterns during directional solidification of bulk samples: Experimental and phase-field studies

F.L. Mota, K. Ji, L. Strutzenberg Littles, R. Trivedi, A. Karma, N. Bergeon

Influence of macroscopic interface curvature on dendritic patterns during directional solidification of bulk samples: Experimental and phase-field studies

F.L. Mota[a], K. Ji[b], L. Strutzenberg Littles[d], R. Trivedi[c], A. Karma[b], N. Bergeon[a]*

[a] *Institut Matériaux Microélectronique Nanosciences de Provence, Aix-Marseille Université and CNRS UMR 7334, Campus Saint-Jérôme, Case 142, 13397 Marseille Cedex 20, France*

[b] *Department of Physics and Center for Interdisciplinary Research on Complex Systems, Northeastern University, Boston, Massachusetts 02115, USA*

[c] *Department of Materials Science and Engineering, Iowa State University, Ames, Iowa 50010, USA*

[d] *NASA Marshall Space Flight Center; Huntsville, AL 35808, USA*

Abstract

The envelope of the solidification front naturally develops a macroscopic curvature in a multitude of solidification processes. However, its effect on dendritic microstructure formation remains poorly understood. Here we exploit a microgravity environment where convection is suppressed to investigate quantitatively the effect of curvature on dendritic array growth during directional solidification of a transparent succinonitrile – 0.46 wt% camphor alloy. In addition, we interpret the results using both theoretical analyses and phase-field simulations. *In situ* observations reveal that even a weak macroscopic interface curvature can have a major effect on both the array pattern evolution and grain structure. First, convex and concave interfaces lead to a continuous increase and decrease in time of the average primary spacing, respectively, which only attains a stationary value for a flat interface. We show that this results from the formation of drifting velocity gradients along the interface under the combined effect of the crystal misorientation and the interface curvature. Second, interface concavity is accompanied by "stray grains" of larger misorientation. These grains form at sample boundaries and overgrow pre-existing interior grains of smaller misorientation to the detriment of well-oriented crystal growth. In addition, they induce a change of array structure when the directional normal to the sample boundary is parallel to one of <100> axis of secondary branches. These results provide new insights for controlling and optimizing directionally solidified alloy microstructures.

Keywords: directional solidification, microgravity experiments, phase-field simulation, pattern formation, interface curvature

* nathalie.bergeon@im2np.fr
+33 (0)4 13 94 52 53

1 Introduction

During alloy solidification, a variety of interface patterns develop when the growth conditions exceed the threshold for the planar interface stability. Pattern selection occurs under dynamic conditions of growth in which the unstable pattern goes through the process of reorganization into a rather periodic array [1] of cells or dendrites. Since the characteristics of patterns strongly influence the properties of the material in solidification processing, it is mandatory to clarify the specific dependence of the solid-liquid interface pattern on processing conditions.

Numerous studies have been directed at predicting the morphological characteristics, and especially the primary spacing, of growing patterns as a function of growth control parameters [2-11]. Most of those studies assume planar interfaces on a large scale. However, solidification processes encountered in nature and application relevant processing usually involve a slight curvature due to large-scale perturbation or instability, or a closed interface geometry. For example, most metallic alloys exhibit macroscopically convex interfaces during solidification as a result of higher thermal conductivity in the solid phase [12].

The effects of solid-liquid interface curvature have been investigated in different fields of material processing. For example, during unidirectional ice-templating of aqueous titanium oxide suspensions [13, 14], a technique to obtain sophisticated structures exhibiting enhanced functionalities, the authors found a disparity in the mean pore width between the outer edge of the sample and its center due to the interface curvature. The pore width, by association with the microstructural characteristics, plays an important role in the material properties. Another example can be found in solidification of binary eutectic alloys. Both experiments and simulations demonstrated the crucial influence of a slight curvature of the isotherms on the long-time dynamics of bulk rod-like eutectic patterns, providing a small symmetry-breaking perturbation in eutectic growth [15]. In the presence of a transverse temperature gradient (or, equivalently, a tilt of the isotherms), the pattern drifts and one of the crucible border becomes a source for new structures. Lamellae formed on this boundary invade the whole interface, leading to the emergence of a regular lamellar array parallel to the transverse temperature gradient direction. The directional solidification of single crystals of Ni-based superalloys which is of major industrial interest for the production of turbine blades is also faced to this problematic. In such alloys, D'Souza et al. observed that the larger the deviation of the local solid-liquid interface from planarity, the larger will be the range of orientations that can occur in the grain texture, thus degrading the quality product [16].

The use of transparent organic analogs, that freeze like metals but are transparent to visible light, is a precious tool for *in situ* observation of the solid-liquid interface [17]. Weiss et al. [18] studied solidification of an organic alloy in a large cylindrical crucible where the solid-liquid interface is curved due to the evacuation of latent heat generated upon solidification through the crucible wall. In such a bulk system, the combination of curvature and convection in the fluid leads to solute macrosegregation and radial variation of microstructure [19] and in cellular arrays, the local interface slope induces pattern advection in which new cells are permanently born, while moving towards the center where they are eventually eliminated [18]. Bottin-Rousseau and Pocheau [20] experimentally investigated the spatiotemporal implications of an artificially curved growth interface in directional solidification of a

transparent alloy in thin sample geometry. Cell advection along the interface slope, associated to stretching, is observed. It induces repetitive cell nucleation by tip-splitting. This phenomenon first occurs in a disordered manner but the cells eventually become ordered over long times and the cell nucleations spontaneously organize themselves in avalanches [21].

The main problem with studying bulk samples comes from the presence of significant convection in the melt. Fluid flow modifies the structure of the solute boundary layer by sweeping, thus causing non-uniform morphological instability with the formation of a non-uniform microstructure and non-uniform primary spacing [19, 22-26]. The easiest way to avoid or drastically reduce convection is to reduce the size of the samples. However, to study bulk samples, the reduced-gravity environment of space is required to eliminate fluid flow. The studies presented here were conducted using the Directional Solidification Insert (DSI) dedicated to *in situ* and real time characterization of the dynamical selection of the solid-liquid interface morphology on bulk samples of transparent materials. The DSI is part of the DECLIC instrument (DEvice for the study of Critical LIquids and Crystallization) and it is installed within the International Space Station (ISS) to benefit from a microgravity environment. It is jointly operated by the French Space Agency (CNES) and NASA. A first series of experiments was performed in 2010-2011, mainly dedicated to cellular growth, which led to unprecedented observations and improvement of numerical models of solidification [27-32]. A second series of experiments was performed in 2017-2018 on a sample of higher solute concentration, dedicated to dendritic growth.

This article reports new experimental results and related phase-field (PF) simulations that quantitatively explore the effects of interface curvature on dendritic patterns. This paper is organized as follows. In the experimental part (Section 2), we first briefly describe the experimental device and methods before describing key characteristics of the growing interfaces, such as macroscopic shapes and the crystallographic orientation of the single crystal. Section 3, dedicated to results, is split into three subsections. The effects of interface curvature in terms of microstructure characteristics are first described, before focusing on its effects on primary spacing. We will provide evidence that the spatial variation of the drifting velocity is at the origin of spatio-temporal structuration of primary spacing. The last subsection will then analyze how the pattern drifting velocity profile is built along the interface. In Section 4, we first describe a quantitative PF model for solidification of dilute binary alloys and the implementation of curved isotherms that induce the macroscopic curvature. Then we present the modeling results and investigate the effects of convex and concave curvatures on the microstructure evolution. Finally, conclusions are summarized in Section 5.

2 Experiments

2.1 Device DECLIC-DSI and experiments

The DECLIC-DSI includes a Bridgman type furnace and the experimental cartridge [33, 34]. Solidification is performed by pulling the experimental cartridge containing the alloy inside the thermal gradient G (between 10 and 30 K/cm) at a pulling rate V ranging between 0.1

and 30 µm/s. The different diagnostics, with illustrations of their specific use, have been previously described in numerous papers, for example in ref. [30, 32, 35]. In the current article, only images obtained by the direct axial observation, providing top-view interface images, and transverse observations, providing side-view interface images, are analyzed.

The organic transparent alloy used is a succinonitrile (SCN) - camphor, with a nominal concentration C_0 = 0.46 wt% camphor. A single crystalline solid seed with a direction <100> parallel to the pulling axial direction is kept unmelted during all experiments. Further details about the experimental procedure can be found in previous works [30, 34, 36].

In this paper, we will focus on a series of experiments performed with a thermal gradient of G = 12.5 K/cm, with a pulling velocity V varying from 1.5 to 12 µm/s. The *in* situ and real time videos corresponding to the solidification experiments are provided as supplementary material [37]. For each experiment, a length of 60 mm is solidified at a constant pulling rate. Whatever the pulling rate is, the formation of the pattern follows the same classical stages described in Figure 1 for V = 3 µm/s, corresponding to snapshots of video2 of supplementary material [37]. Selected top-views of the solid-liquid interface at different times are given in Figure 1. The corresponding side-views illustrate the recoil of the interface within the furnace, associated to the curvature change, similar to previous studies [30]. We start from rest (V = 0, t = 0), with a smooth and convex interface (Fig. 1a). After triggering of the pulling, we first observe a rather complex array of more or less linear ridges along sub-boundaries followed by the development of a more or less uniform corrugation within the sub-grains (Fig. 1b). The interface dynamics is very fast and interface modulations amplifies to eventually lead to a clear but highly disordered dendritic pattern (Fig. 1c). The dynamics then slows down, and a stage of continuous pattern evolution starts (Fig. 1d). In this paper, we will concentrate on this last stage. The dendritic patterns after 45 mm of pulling are illustrated in Figure 2a for the different velocities (only 20 mm for V = 12 µm/s). They obviously differ in primary spacing that becomes finer when the pulling velocity increases. Additionally, it is worth noting that parasite sub-grains coming from the crucible border progressively invade the well-oriented central grain for pulling rates higher than 3 µm/s. The parasite sub-grains are characterized by a higher misorientation of their dendrite growth direction; they are then more tilted so that the light is more diffused and sub-grains appear darker than the well-orientated central grain (see the videos of [37] to clearly visualize this phenomenon). The higher the pulling rate is, the faster the invasion is: at V = 12 µm/s after 37 mm of solidification the central grain has almost vanished.

The pattern is characterized in terms of primary spacing and order/disorder level. Each structure of an image is first identified and labeled before applying a Voronoi tessellation to identify the first neighbors. Primary spacing corresponds to the average of the center-to-center distances of a structure with its first-neighbors. Each dendrite is tracked from one image to the following, so that its possible motion (drift in the interface plane) can be analyzed (trajectory, velocity). More details on the methods of data treatment can be found elsewhere [38].

On the videos of supplementary material [37], the most striking observation is that, seen from the top, dendrites are drifting in the interface plane, with characteristics that depend on pulling velocity as stated in Figure 2b. Drifting velocity maps are given for each velocity

after 30 mm of pulling, where the individual drift velocity of each dendrite defines its color. The corresponding drifting direction maps were also obtained, and the arrows superposed to Figure 2b correspond to drift velocity vectors. At 3 µm/s the drift is roughly homogeneous in value and direction on the whole interface. For the other pulling rates, the main direction of drift remains the same from top left to bottom right but its spatial homogeneity is modulated differently with pulling rate. At V = 1.5 µm/s, dendrites tend to move towards the border and the drifting velocity increases towards the bottom and the right; at V = 6 and 12 µm/s, dendrites tend to move towards the center and the drifting velocity decreases towards the bottom and the right. The origin of the drifting characteristics and its consequence on pattern are analyzed in §3.

2.2 Macroscopic interface shape

Macroscopic shape and motion of the interface are investigated by side view observation. The macroscopic interface shape is a consequence of the isotherms' shape that is usually curved in 3D configurations. Here, we assimilate the "interface" to the liquidus isotherm at rest, and to the cell/dendrite tips isotherm while pulling. Seen from the side, the interface appears as a curved line that can generally be fitted by a parabola. The interface curvature can be quantified by the curvature radius of the parabola or by the "interface amplitude" that corresponds to the difference between the interface positions measured in the center and on the border of the crucible. With this second method of quantification, positive and negative values respectively correspond to convex and concave interfaces. Side view images of the solid-liquid interface are given in Figure 3a, at rest and during pulling, for different velocities, where one can easily distinguish the liquid and solid part of the sample.

The origin of curvature and the analysis of its evolution while pulling has been largely discussed in a previous paper [30] and present experiments are consistent with the key points already reported. In Figure 3a, the interface at rest is convex. While pulling, the interface recoils and its shape becomes more and more concave as pulling velocity increases. So, we observe that: at V = 1.5 µm/s, the interface is still convex but less than at rest; it is macroscopically flat at 3 µm/s; and it becomes slightly concave at 6 µm/s. For concave interfaces, the central part of the interface (at a lower position) is hidden from the side camera view by the dendrites at the crucible wall (at a higher position). Consequently, the interface shape is not clearly visible, as shown in Figure 3a for V = 6 µm/s. At V = 12 µm/s, the interface is out of the field of view.

The software package CrysMAS® designed for the global modeling of solidification processes in complex furnaces is used here to compute the thermal field and study the interface position and shape, as detailed in [30]. Figure 3b gives the interface shapes in the adiabatic area calculated with CrysMAS® for the experimental conditions. At V = 1.5 µm/s, the experimental side view of the interface at steady-state allows to determine the interface shape, which is additionally represented in Figure 3b. The experimental shape superposes well to the calculated one, thus validating the numerically determined shapes. Experimental shapes will be used when available, as for V = 1.5 and 3 µm/s; shapes extracted from CrysMAS simulations will be used for other cases, at V = 6 and 12 µm/s.

2.3 Crystallographic orientation

A single crystal seed is used, with a <100> direction aligned with the pulling axis as closely as possible. The experiments described in this work were performed sequentially and it was clearly observed that, in the early stages of solidification, the "well-oriented" sub-grain dominates. Stray sub-grains may progressively invade the central area at large velocities, but we will focus on the dendrite behavior in the central well-oriented grain.

The growth direction of a cell/dendrite rotates from the thermal gradient direction at a low velocity to the closest <100> direction as the pulling rate increases [39, 40]. A sub-grain is characterized by a collective drift of the structures, of specific direction and amplitude, caused by its particular misalignment to the pulling/thermal axis. To determine the orientation of the central grain, we measure the drifting velocity for a flat interface (at V = 3 μm/s). The average amplitude of drift velocity $\overrightarrow{V_d}$ is used to evaluate the tilt angle θ_g between the growth velocity $\overrightarrow{V_g}$ and the vertical interface velocity $\overrightarrow{V_I} = -\vec{V}$. For a flat interface, the thermal gradient $\vec{G}$ is parallel to the interface velocity as shown in the configuration ② of Figure 4a, and the tilt angle θ_g is simply determined by the relation:

$$\tan\theta_g = \frac{V_d}{V} \quad (1)$$

The misorientation of a sub-grain is defined by the angle θ_o between the preferred <100> growth direction (noted as $\vec{a}$ in Figure 4) and $\vec{G}$. The cell/dendrite growth direction varies relatively to θ_o, and this variation depends on the Péclet number $Pe = \lambda V/D$ (where λ is the primary spacing and *D* is the solute diffusion coefficient in the liquid) and is generally described by a phenomenological equation [39, 41-43]:

$$\frac{\theta}{\theta_o} = \frac{1}{1+fPe^g} \quad (2)$$

where θ is the angle between the preferred <100> direction and the growth direction, *f* and *g* are two fitting constants. Equation (2) was previously used to describe the drifting dynamics under a flat interface with the local interface slope $\alpha = 0$, for which $\theta_0 = \theta_g + \theta$. Here, we also use it to describe the drifting dynamics under a curved interface with α varying at different positions and assume that *f* and *g* are independent of curvature.

As illustrated in Figure 4a, the growth direction $\overrightarrow{V_g}$ always lies between the thermal gradient $\vec{G}$ and the preferred <100> direction $\vec{a}$ for different interface slopes. For a given value of Pe, the ratio θ/θ_o is constant, so that when θ_o increases due to the variation of α, θ also increases and the drifting velocity decreases, as described in Figure 4a.

We use the 3D PF simulation and the method described in Refs. [29, 31, 32] to determine *f* and *g* values associated to the SCN-0.46 wt% camphor alloy, with growth conditions $G = 12\ \mathrm{K/cm}$ and $V = 1.5\text{ - }12\ \mu\mathrm{m/s}$. In the PF simulation, we construct a regular hexagonal array with a flat interface and impose a constant crystallographic tilt angle $\theta_0 = 2°$ (*f* and *g* are independent of θ_0 according to [44]). The dendritic array drifting due to misorientation is fitted by Eq. (2), which gives the *f* and *g* values at different pulling velocities. As a result, we

obtain f = 1.13 and g = 1.38 for V = 1.5 $\mu m/s$; f = 0.62 and g = 1.80 for V = 3 $\mu m/s$; f = 0.42 and g = 1.76 for V = 6 $\mu m/s$; f = 0.60 and g = 1.35 for V = 12 $\mu m/s$.

Based on the experimentally measured average primary spacing $\overline{\lambda} = 468\,\mu m$ and the average drifting velocity $\overline{V_d} = 0.13\,\mu m/s$, together with the PF-determined f and g, the crystal misorientation θ_o = 2.7° was obtained for V = 3 µm/s when the interface is flat. For the other pulling velocities when interfaces are curved, we use Eqs. (1)-(2) in the central region where the interface is locally flat to calculate θ_o. The same value θ_o = 2.7° was obtained for V = 1.5 and 6 µm/s.

3 Results

3.1 Microstructure characteristics

The question here is to determine how the pattern organization is affected by the drifting and curvature.

First, let us focus on the central well-oriented grain. Whatever the pulling rate is, the maps of numbers of first neighbors are similar. They reveal a hexagonal basis, with numerous defects (mainly pairs of 5 – 7 neighbors) and high disorder. Such disordered hexagonal arrays are typical of solidified cellular patterns [28, 45], and they also appeared dominant in large scale 3D PF simulations [46]. It is experimentally observed that in spite of the cubic symmetry which is a determinant for the secondary branches' formation, the dendritic pattern organization does not obviously reflect the crystal anisotropy and the spatial ordering seems similar to the natural hexagonal structure observed for cellular structures.

Regarding the grain structure, these experiments reveal a very striking consequence of concave curvature. At V = 1.5 µm/s and 3 µm/s, convex and flat interfaces respectively, no major evolution of the grain structure is observed: only one major grain is observed without stray grains invasion. However, when the interface is concave, at V = 6 and 12 µm/s, the central region containing the well-oriented grain is invaded by sub-grains coming from the crucible border. These invading sub-grains, or stray grains, are characterized by various drifting directions as well as a large range of drifting velocities (Figure 5a and b), generally higher than the average drifting velocity of the central well-oriented sub-grain thus witnessing of a higher misorientation. It means that the concavity favors the formation and propagation of stray grains characterized by off-axis crystallographic orientations.

At V = 6 µm/s (Figure 5a), all stray grains originate upstream of the central grain (from the top and left image sides). They drift in roughly the same direction but their higher velocities define convergent sub-boundaries with the central grain. At V = 12 µm/s (Figure 5b), stray grains also invade from the bottom side of the image: with a drift direction roughly opposite to the central grain so that convergent sub-boundaries are also formed. In both cases, it appears that the central grain is overgrown by these stray grains, in spite of its lowest misorientation. This is in contradiction with the classical conjecture that the best oriented grain cannot be overgrown and the grain boundary follows the growth direction of the most favorably oriented grain. This conjecture has been formalized and justified by Walton and

Chalmers [47] on the basis of the lower undercooling of a grain with lower misorientation with respect to the thermal gradient compared to neighboring grains with higher misorientation. Unusual overgrowth of favorably oriented dendrites at converging grain boundary has already been reported [48-51], but Tourret et al. [52] have found that it is rare and limited - for low misorientations similar to our case - to some convergent boundaries with opposite drifting directions. Our observations indicate that curvature favors the occurrence of this unusual phenomenon and extends the conditions of its appearance to other types of converging boundaries: in the case of curvature, it even occurs for convergent boundaries with the same drifting directions.

At 12 µm/s, the final grain texture resulting from the complete overgrowth of the initial central grain is formed by several off-axis grains. Such an observation has been reported previously by D'Souza et al. [16] in the case of directional growth of Ni-based superalloys that present a concave interface: post-mortem texture analyses evidence that the larger the concavity is, the wider the range of orientations in the final texture. A possible interpretation, proposed by the authors, is that the orientation of the local gradient varies in a curved interface so that the most favored orientation varies all along the interface. Our observations invalidate this proposition as it cannot explain the continuous propagation of off-axis grains. They keep propagating and overgrowing the central well-oriented grain during their whole drift that starts at the border and ends in the center while the thermal gradient orientation varies continuously during this motion. The final texture formed by off-axis grains results from a general unusual overgrowth phenomenon favored by concavity.

The last point to discuss regarding the microstructure is the appearance of an unusual pattern organization at V = 6 and 12 µm/s in some areas of the stray grains. These areas are noted from 1 to 4 in Figure 5b and are enlarged in Figure 5c. The classical organization of a tilted dendritic pattern is visible, for example, in area 0 of Figure 5b and c. The effect of tilt is mainly to modify the 4th order symmetry appearance in top-view observation by hiding half of the dendrite. 3D phase-field simulations of misoriented dendritic patterns lead to similar microstructures as for example in Fig. 1 of Takaki et al. [53]. In area 0, no specific ordering appears. On the other hand, in areas 1 to 4, dendrite primary trunks are aligned along the directions of the secondary branches, indicated by the yellow and blue dashed lines. It is worth noting that these aligned dendrites were not present and visible at the beginning of the pattern formation: they probably were formed after the initial transient along the border (out of visibility) then propagated towards the center and became visible. The location of the different areas with respect to the crucible border is schematically given in Figure 5d, together with the two directions of secondary branches in yellow and blue dashed lines. The secondary branches of the aligned structures in areas 1 to 4 are normal to the crucible border. At these locations, a tilted dendrite that drifts away from the border will be associated to a periodic source via a tertiary branching process, with a quite similar mechanism observed in thin samples of tilted patterns by Song et al. [43]. The aligned structures of areas 1 to 4 result from the propagation of these periodically generated dendrites. In area 0, the tilted dendrites that drift far from the border are also sources. But as the orientation of secondary branches regarding the crucible border is not specific, the tertiary branching is neither locked on the secondary branches nor periodic. As will be discussed in Section 4.2.3, the aligned structure caused by the invasion of dendrites from the source at the border can also be observed in the

3D PF simulation. It is worth noting that we observed such arrangements in all dendritic experiments, whatever the experimental parameters are (concentration, thermal gradient, pulling velocity) as soon as the interface is concave and the drifting velocity is high enough to induce the formation of several dendrites by tertiary-branching at the border. We believe that this arrangement is very difficult to detect by post-mortem analysis, thus explaining that it has never been reported.

3.2 Primary spacing evolution

Figure 6 shows the time evolution of primary spacing for the different pulling velocities. Those measurements are limited to the well-oriented grain and they start after the initial transient that leads to the formation of the well-developed pattern; during this earlier stage, the primary spacing increases. For V = 12 µm/s, the well-oriented grain disappears after 36.8 mm of growth, thus explaining the early stop of the curve. As usual in a solidification pattern, a band of primary spacing is observed; minimum and maximum values of spacing are also represented on the graphs of Figure 6. It is well-known that a wide band of stable spacings exists, limited by elimination at its lowest value and tertiary branching for dendritic array at its largest value [5, 7, 10, 54-59]. However, in our measurements, the minimal and maximal spacing values do not correspond to limits of the stable spacing band as elimination or tertiary branching do not occur in the central well-oriented grain, but may sometimes be observed in the frame of competition with invading grains at the sub-boundary.

Regarding the average spacing curve for each velocity (Figure 6), a striking difference appears. At V = 3 µm/s, the average spacing stabilizes after the initial transient stage whereas for the other pulling velocities, it keeps evolving during the whole solidification. At V = 1.5 µm/s, the spacing increases with time; at V = 6 and 12 µm/s, it decreases. This difference in evolution can be linked to the macroscopic interface curvature inversion from convex at V = 1.5 µm/s to concave when V is higher than 3 µm/s. For convex interfaces, Bottin-Rousseau et al. [20] evidenced a progressive stretching of cells while they drift from center to border that eventually led to tip-splitting when the upper stable limit is reached. Inversely for concave interfaces, still for cellular patterns, Weiss et al. [36] evidenced and analyzed the size decrease of cells while they drift from the border toward the center. It appears here that similar behaviors occur in the dendritic patterns.

To better understand the origin of this variation, we analyzed the spatial homogeneity of the spacing with time for V = 1.5 µm/s. This experiment is chosen as the spacing evolution is large and due to convexity, no invading sub-grain enters the studied area. So, rather than consider the whole interface as in Figure 6, nine small areas of interest A_i are defined as described in Figure 7a. In each area A_i, measurements of spacing and drifting velocity are performed on all dendrites of the area (average of 20 dendrites per area) and repeated every 170 s (step of 250 µm of growth). The average spacing evolution during the second third of the solidification (from L = 20 to 40 mm) was measured in each area and the variation in % is given in Figure 7b. We note that even if the spacing increases everywhere, its increase is larger in central and bottom right areas (A5-A6-A8-A9).

The origin of cell stretching/reduction is linked to a variation of the drifting velocity along the interface [20, 36]. In the case of a misoriented dendritic pattern on a flat interface, at V =

3 µm/s, the primary spacing remains stable and the analysis of drifting velocity reveals a homogeneity of drifting velocity all along the interface (Figure 2b). However, at V = 1.5 µm/s, on a convex interface, the drifting velocity map reveals large variations along the interface. The average drifting velocity in each area A_i was measured and compared to the average considering the whole interface. Figure 7c represents the respective differences in each area, where the arrows indicate the drifting direction and their length is proportional to the velocity. A very clear and strong drifting velocity gradient appears along the diagonal A1-A5-A9. This gradient is roughly parallel to the drifting direction. Still along drifting direction, we notice strong gradients along A1-A4-A7, A4 & A5 to A8 and A2 to A6. The downward motion along the drifting direction, associated to gradients of drifting velocity, induces the dendrite stretching and so the large increase of spacing in A4 to A9 (Figure 7b).

As demonstrated here, the spatial variation of drifting velocity is at the origin of spatio-temporal structuration of primary spacing. It is then worth studying the formation of the drifting velocity profile along the interface.

3.3 Local curvature and drift

The effect of curvature on cellular patterns has been previously described respectively for convex [20] and concave [36] interfaces. A phenomenon of advection appears that drives cells to drift along the interface slope. This advection is linked to the existence, due to the curvature, of an angle between the imposed pulling rate and the thermal gradient which is normal to the interface. Cells grow perpendicular to the solid–liquid interface as long as the growth direction is not tilted by anisotropy. Thus, the cell growth velocity has a radial component which in top view makes them drift down the interface slope.

In the present case, dendritic patterns grow with misorientation on a curved interface. To roughly visualize the combined effects of curvature and of crystalline misorientation in terms of pattern drift, we can first suppose that each effect induces its own drifting contribution and the resulting drift is just their addition. Even if this approach is not completely correct, it highlights the main characteristics of drifting velocity fields. The different contributions are drawn in Figure 8 for convex and concave interfaces. Misorientation induces a translational drift which is constant all along the interface (green arrows) on a macroscopically flat interface. On a curved interface, advection induces an axisymmetry (blue arrows), towards the periphery for a convex interface and towards the center for a concave one, and its component increases when distancing from the center. The resulting drifting velocity is represented by the red arrows. Comparing with the flat interface case where the drifting velocity field is constant all over the interface, the interface curvature induces a divergence of the drifting velocity field for a convex interface and a convergence for a concave one. Also, gradients of drifting velocity are built due to curvature. This structuration of the drifting velocity field is consistent with our observations, given in Figure 2b.

This approach should be corrected as the variation of the growth velocity direction with respect to the orientation of thermal gradient and misorientation - described by Eq. (2) and Figure 4 - is not considered. A better model can be done in the plane resulting from the transverse interface cutting along the drifting direction, i.e. along the orange line (AB) of Figure 8. We then obtain interface profiles schematically drawn in Figure 4b. For a convex

interface (V = 1.5 µm/s), if one goes from A to B, it means going from configurations ③ to ② to ① of Figure 4a, and the resulting drifting velocity simultaneously increases. For a slightly concave interface (V = 6 µm/s), going from A to B means going from configurations ① to ② to ③, and the resulting drifting velocity simultaneously decreases. For a highly concave interface (V = 12 µm/s), we can reach configuration ④ which is associated to an inversion of the drifting velocity. This was experimentally observed with the drift velocity of the stray grains around point B for V = 12 µm/s (Figure 5b).

Equation (2) can be applied to the experimental interface shape to get the theoretical variation of drifting velocity along the interface, from A to B. The interface shapes given in Figure 3 can be fitted by $z(r) = ar^2 + b$, where *z* is the height, *r* the distance from the center and, *a* and *b* fitting constants. The local interface slope $\alpha(r)$ can be determined by the *z(r)* derivative. The local misorientation $\theta_0(r)$ is linked to α: $\theta_0(r) = \theta_{0_P} + \alpha(r)$, with θ_{0_P} the misorientation for a flat interface (θ_{0_P} = 2.7° as mentioned in §2.3). Moreover, with the relation $\theta(r) = \theta_{0_P} - \theta_g$ and Eq. (2), we obtain:

$$\theta_g(r) = \theta_{0_P} - \frac{\theta_{0_P} + \alpha(r)}{1 + fPe^g} \qquad (3)$$

Equation (1) can also be adjusted to calculate $V_d(r)$ for a curved interface as follows:

$$\tan\left(\theta_g(r)\right) = \frac{V_d(r)}{V_I + V_d(r)\tan\alpha(r)} \Leftrightarrow V_d(r) = \frac{V_I \tan\left(\theta_g(r)\right)}{1 - \tan\alpha(r)\tan\left(\theta_g(r)\right)}, \qquad (4)$$

where $\theta_g(r)$ can be calculated by Eq. (3) with a given set of *f* and *g* values.

We compare the results of such calculations to experimental measurements of drift velocities at V = 1.5 and 6 µm/s in Figure 9. The dendrites included in the measurements are marked in red in Figure 9a and d; they are chosen along the interface diagonal to represent an interface cut. The experimental data of drift velocities (Figure 9c and f) and primary spacing (Figure 9b and e) come from five close images to reduce the dispersion which is unavoidable as only a few dendrites are located in the interest area, and curves are drawn using a sliding average calculated on eight successive points. The theoretical profiles of the drifting velocity in these figures have been calculated using Eq. (4) with local Peclet number calculated using experimental primary spacing curves of Figure 9b and e.

For V = 1.5 µm/s, the experimental and calculated curves superpose almost perfectly, thus validating the chosen approach to combine misorientation and curvature and evaluate drifting velocity. For V = 6 µm/s, the experimental variation is quite well reproduced by calculation in the central area, for *r* roughly between 0- and 3-mm. Curves strongly deviate in other areas. For the top left area, the deviation can be explained by the invasion of stray grains of higher drifting velocity. In the bottom right area, the discrepancy may come from a border effect which leads to an abrupt slow-down. It should also be remembered that, contrary to V=1.5 µm/s, the shape of the interface at 6 µm/s is not determined experimentally but from the profiles simulated in CrysMAS. The sensitivity of these

calculations to the curvature is extremely important. For example, if for V = 1.5 μm/s the calculation is done with the curvature extracted from the CrysMAs data and not from the experimental data, then the experimental variation of the drift velocity is twice the calculated one. There is thus a significant uncertainty on the exact value of the curvature in the case V = 6 μm/s which can also largely explain the observed differences.

4 Phase-field modeling with macroscopic interface curvature

Computational modeling of the DECLIC experiments for directional solidification of a transparent dilute alloy to date has focused exclusively on observations obtained in a velocity range where the solidification front is flat [26, 28, 29, 31, 32]. However, solidification fronts with a macroscopic curvature are frequently observed [30]. In this section, by implementing a radial temperature gradient into the quantitative PF model, we can initiate a macroscopically convex or concave interface during PF simulations and investigate its long-time effects on the microstructure evolution. We first describe a quantitative phase-field model for solidification of dilute binary alloys that is applicable to different thermal conditions in Section 4.1.1, then we introduce the temperature field with a radial gradient in Section 4.1.2 and the numerical implementation in Section 4.1.3. The results of PF simulations are discussed in Section 4.2, including the effects of curvature on the primary spacing evolution (Section 4.2.1), the drifting dynamics of misoriented cells under a curvature (Section 4.2.2), and the pattern organization (Section 4.2.3).

4.1 Model, simulations, and parameters

4.1.1 Model equations

We use a well-established quantitative PF model [60, 61] for solidification of dilute binary alloys that is applicable to different thermal conditions. The model equations are

$$F_1(\boldsymbol{r},t)a_s(n)^2\frac{\partial\psi}{\partial t} = a_s(n)^2\left(\nabla^2\psi - \varphi\sqrt{2}\left|\vec{\nabla}\psi\right|^2\right) + \vec{\nabla}[a_s(n)^2]\cdot\vec{\nabla}\psi \qquad (5)$$
$$+\sum_{q=x,y,z}\left[\partial_q\left(\left|\vec{\nabla}\psi\right|^2 a_s(n)\frac{\partial a_s(n)}{\partial(\partial_q\psi)}\right)\right] + \sqrt{2}[\varphi - \lambda(1-\varphi^2)F_2(\boldsymbol{r},t)],$$

and

$$(1+k-(1-k)\varphi)\frac{\partial U}{\partial t} = \tilde{D}\vec{\nabla}\cdot\left[(1-\varphi)\vec{\nabla}U\right] + \vec{\nabla}\cdot\left[(1+(1-k)U)\frac{(1-\varphi^2)}{2}\frac{\partial\psi}{\partial t}\frac{\vec{\nabla}\psi}{|\vec{\nabla}\psi|}\right] \qquad (6)$$
$$+[1+(1-k)U]\frac{(1-\varphi^2)}{\sqrt{2}}\frac{\partial\psi}{\partial t},$$

where $F_1(\boldsymbol{r},t)$ and $F_2(\boldsymbol{r},t)$ are two functions depending on thermal conditions. Here φ is the PF that takes on constant values in solid $(+1)$ and liquid (-1) and varies smoothly across the diffuse interface, and ψ is a nonlinear preconditioning PF defined as $\psi = \tanh(\varphi/\sqrt{2})$. A dimensionless supersaturation field U is coupled to the PF, with the definition

$$U = \frac{1}{1-k}\left[\frac{c/c_l^0}{(1-\varphi)/2+k(1+\varphi)/2} - 1\right], \qquad (7)$$

where k is the interface solute partition coefficient, c is the solute concentration in molar fraction, $c_l^0 = (T_m - T_0)/|m|$ is the liquidus concentration at the reference temperature $T = T_0$, with T_m the melting temperature of pure solvent and m the liquidus slope. The length and time are scaled by the diffuse interface thickness W and the relaxation time τ_0 [60, 61], respectively. The dimensionless diffusivity $\widetilde{D}$ in Eq. (6) is given by $\widetilde{D} = D\tau_0/W^2 = a_1 a_2 W/d_0$, where $a_1 = 5\sqrt{2}/8$ and $a_2 = 47/75$. The capillary length d_0 is defined at the reference temperature T_0 by $d_0 = \Gamma/|m|(1-k)c_l^0$, with Γ the Gibbs-Thomson coefficient of the solid-liquid interface. The coupling factor is $\lambda = a_1 W/d_0$. We consider a standard fourfold anisotropy of the interface free-energy, $\gamma(\alpha) = \gamma_0 a_s(\boldsymbol{n}) = \gamma_0(1+\epsilon_4\cos 4\,\alpha)$, where γ_0 is the average interface free energy in the $\langle 100\rangle$ plane, ϵ_4 is a measure of the strength of the anisotropy, and α is the angle between the local surface normal vector and a fixed crystalline axis. For a crystal orientation angle θ_0 with respect to the reference axis, the anisotropy function in the PF model is $a_s(\boldsymbol{n}) = 1+\epsilon_4\cos[4(\alpha-\theta_0)]$. We impose the misorientation angle θ_0 in PF simulations using the rotation matrix method with details given in [52].

4.1.2 Temperature field

We consider a 2D temperature field $T(x,y)$ for a thin-sample geometry, which can also represent the thermal condition for the cross-section of a 3D cylindrical sample that is parallel to the pulling velocity. With the assumption that the temperature field does not vary with time, $T(x,y)$ can be described by

$$T(x,y) = T_0 + Gx + T_r(y), \quad (8)$$

where G is a constant temperature gradient directed along the vertical x-direction, $T_r(y)$ is a function that describes the radial temperature variation along the y-direction, T_0 is a reference temperature at $x = 0$ and $T_r(y) = 0$. When $T_r(y) = 0$, Eq. (8) reduces to a classical frozen temperature approximation in one dimension. Here, we consider a parabolic shape of the isotherm $x = x_0 + A(y/L - 1/2)^2$ with extrema at the sample center $y = L/2$, where x_0 is an arbitrary reference position, A is a measure of the amplitude of the macroscopic curvature, L is the sample size in the y-direction, and $0 \le y \le L$. Then, we can obtain $T_r(y) = \Delta T_r(y/L - 1/2)^2$, where $\Delta T_r = -AG$ is proportional to the maximum variation of the radial temperature at a given sample height. In PF simulations, we use a value $A = -972\ \mu\mathrm{m}$ for a convex interface at $V = 1.5\ \mu\mathrm{m/s}$ obtained from the direct experimental observations of the interface shape. However, as explained in section 2.2, the interface shape of a concave interface cannot be directly observed from the side view in the DECLIC experiment because the lower center is obscured by dendrites near the crucible boundary. Thus, we use a value $A = 284\ \mu\mathrm{m}$ obtained from the CrysMAS® simulation for a concave interface with DECLIC experimental conditions at $V = 6\ \mu\mathrm{m/s}$.

To incorporate the temperature field into the PF model, we use the thermal conditions in Eq. (5):

$$F_1(x,y,t) = 1-(1-k)\frac{x+A\left[1/4-(y/L-1/2)^2\right]-\tilde{V}_p t}{\tilde{l}_T}, \quad (9)$$

and

$$F_2(x,y,t) = U+\frac{x+A\left[1/4-(y/L-1/2)^2\right]-\tilde{V}_p t}{\tilde{l}_T}, \quad (10)$$

where x, y, and A are scaled by the diffuse interface thickness W, and t is scaled by the relaxation time τ_0. The dimensionless pulling velocity $\tilde{V}_p$ and thermal length $\tilde{l}_T$ in Eqs. (9)-(10) are defined by $\tilde{V}_p = \frac{V_p \tau_0}{W} = a_1 a_2 \frac{V_p d_0}{D}\left(\frac{W}{d_0}\right)^2$ and $\tilde{l}_T = \frac{l_T}{W} = \frac{l_T}{d_0}\frac{1}{W/d_0}$, where $l_T = |m|(1-k)c_l^0/G$ is the dimensional thermal length.

4.1.3 Implementation

We solve Eqs. (5)-(6) on a cubic lattice of grid spacing Δx using a finite-difference implementation of spatial derivatives and an Euler explicit time stepping scheme with a constant time step Δt. The spatial discretization utilizes a simple seven-point stencil that contains six nearest-neighbor points in ⟨100⟩ directions on a cubic lattice [62]. The PF model is solved on massively parallel graphic processing units (GPUs) with the computer unified device architecture (CUDA) programming language. In addition, we use the multi-GPU technique to improve the efficiency of large-scale simulations [32].

We perform numerical simulations for directional solidification of a SCN-0.46 wt% camphor alloy with the DECLIC experimental conditions, including the temperature gradient directed along the vertical x-direction $G = 12\ \mathrm{K/cm}$ and the pulling velocity $V = 1.5$ and $6\ \mu\mathrm{m/s}$. The alloy parameters include the partition coefficient $k = 0.1$ the liquidus slope $m = -1.365\ \mathrm{K/wt\%}$ [63], the diffusion coefficient $D = 270\ \mu\mathrm{m}^2/\mathrm{s}$, and the crystalline anisotropy $\varepsilon_4 = 0.011$. The numerical parameters are chosen to be the interface thickness $W/d_0 = 185$, the grid spacing $\Delta x/W = 1.2$, and the explicit time step $\Delta t \approx 0.0036\ s$ for simulations at $V = 1.5\ \mu\mathrm{m/s}$; $W/d_0 = 165$, $\Delta x/W = 1.2$, and $\Delta t \approx 0.0028\ s$ for simulations at $V = 6\ \mu\mathrm{m/s}$. In the following sections, the simulation domain size of a thin-sample geometry is $L_x \times L_y \times L_z = 2026 \times 7800 \times 100\ \mu\mathrm{m}^3$ for simulations at $V = 1.5\ \mu\mathrm{m/s}$, and $L_x \times L_y \times L_z = 900 \times 7800 \times 100\ \mu\mathrm{m}^3$ for simulations at $V = 6\ \mu\mathrm{m/s}$, where $L_z = 100\ \mu\mathrm{m}$ is the sample thickness in the z-direction. We consider wetting boundary conditions where a layer of liquid is systematically wetting the sample walls at $y = 0$, $y = L_y$, $z = 0$, and $z = L_z$. Since the triple line where the solid-liquid interface contacts with the sample wall is located deep within the mushy zone, we choose a simplified description of the wetting boundary condition by forcing a contact angle of the interface with the walls on the nearest layer of grid points next to the sample walls, with details given in [52]. Initially, we create a curved interface with a parabolic shape at the liquidus temperature, which also matches the isotherm shape. The simulated time is set to 10 hours, which takes approximately 10 and 20 days of computation time with two Nvidia V100 GPUs for simulations at $V = 1.5$ and $6\ \mu\mathrm{m/s}$, respectively. We also perform PF simulations in a 3D bulk sample, as will be discussed in Section 4.2.3.

4.2 Results of simulations

4.2.1 Primary spacing evolution

We investigate the evolution of the primary spacing under the influence of the macroscopic curvature in PF simulations where a well-oriented single crystal grows in the thin-sample geometry. Figure 10a shows a macroscopically convex interface in the PF simulation at $V = 1.5\ \mu\mathrm{m/s}$. The locations of cell tips (dots) in the central region follow well the isotherm shape (curves) described by Eq. (8) with $A = -972\ \mu\mathrm{m}$, which indicates that cell tips still grow at the same temperature under a weak macroscopic curvature. For a few cells near the simulation boundaries, their tips are located slightly below the isotherm that passes through most cell tips in the central region, and those cells at the boundaries are eliminated due to the wetting boundary conditions applied at $y = 0$ and $y = L_y$. Under the influence of the convex interface curvature, cells drift laterally towards the boundaries, and the evolution of the primary spacing λ can be significantly affected by the curvature over a long period of time. Figure 10b shows the spatiotemporal evolution of λ in the simulation of Figure 10a, where we only measure cell tips that are at least 200 $\mu\mathrm{m}$ away from the simulation boundaries in the y-direction. At an early time t_1, the λ value is unevenly distributed. Then, λ increases over time across the entire simulation domain, and its spatial distribution becomes smoother. At a time $t \geq t_3$, λ has lower values near the simulation boundaries and a maximum value at the sample center. As shown in Figure 11a, the average primary spacing λ_{ave} increases as cells are eliminated at the boundaries. Meanwhile, both the maximum spacing λ_{max} found at the sample center, and the minimum spacing λ_{min} found near the boundaries increase over time, which is in good qualitative agreement with the experimental observation in Figure 5 for $V = 1.5\ \mu\mathrm{m/s}$.

Figure 10c shows a macroscopically concave interface in the PF simulation at $V = 6\ \mu\mathrm{m/s}$. In this case, the locations of cell tips (dots) follow well the isotherm shape (curves) described by Eq. (8) with $A = 284\ \mu\mathrm{m}$, and the effects of the simulation boundaries are small. Figure 10d shows the spatiotemporal evolution of λ in the simulation of Figure 10c, where we only measure cell tips that are at least 150 $\mu\mathrm{m}$ away from the simulation boundaries in the y-direction. At an early time t_1, the primary spacing λ is unevenly distributed and has a local maximum near the sample center. Under the influence of the concave interface curvature, cells drift laterally towards the sample center, and λ near the sample center decreases. Meanwhile, λ near the right boundary slowly increases over time. At a later time t_5, λ has the minimum value near the sample center and higher values near simulation boundaries. As shown in Figure 11b, the average primary spacing λ_{ave} does not change significantly, while both λ_{max} and λ_{min} slightly decrease over time. This observation partially agrees with the experimental observation in Figure 6 for $V = 6\ \mu\mathrm{m/s}$, where λ_{ave} in the latter decreases visibly over time. One possible explanation is that the value $A = 284\ \mu\mathrm{m}$ obtained from the CrysMAS® simulation for an interface at rest underestimated the magnitude of the concave curvature at $V = 6\ \mu\mathrm{m/s}$. Thus, the curvature effects are potentially smaller in the PF simulation than the experiments.

4.2.2 Drifting dynamics

We investigate the drifting dynamics that usually results from the combined effects of macroscopic curvature and crystal misorientation in experiments. Here, we consider a macroscopically curved interface for a tilted array in a thin-sample geometry. Figure 12a shows the distribution of cell drifting velocity V_d in a PF simulation at $V = 1.5\ \mu\mathrm{m/s}$, where the interface is macroscopically convex and the crystalline misorientation angle is $2.7°$. Since the crystalline misorientation has a larger effect than the convex curvature, all cells drift towards the right side, i.e., in the same direction of the misorientation. The measured V_d profile (solid line in blue) increases from left to right, and a velocity gradient that prevents a stationary pattern can be clearly observed. This velocity gradient is caused by the fact that the cell drifting is suppressed by the convex curvature on the left side of the simulation domain, while the drifting is favored by the convex curvature on the right side as analyzed in section 3.3. The measured V_d profile is compared to the calculated V_d profile using Eq. (4) (dashed line in red), where the local primary spacing and the constants fitted for a flat interface ($f = 1.13$ and $g = 1.38$ for $V = 1.5\ \mu\mathrm{m/s}$) were used to determine the local drifting velocity.

Figure 12b shows the distribution of cell drifting velocity V_d in a PF simulation at $V = 6\ \mu\mathrm{m/s}$, where the interface is macroscopically concave with a misorientation angle $2.7°$. All cells drift in the same direction of the misorientation, and the measured V_d profile (solid line in blue) decreases from left to right. This is because the cell drifting is favored by the concave curvature on the left side of the simulation domain, while the drifting is suppressed by the concave curvature on the right side. The measured V_d profile is compared to the calculated V_d profile using Eq. (4) with $f = 0.42$ and $g = 1.76$ for $V = 6\ \mu\mathrm{m/s}$.

For both convex and concave interfaces, a reasonably good overall agreement is found between the V_d profiles measured in PF simulations and calculated using Eq. (4). In both cases, however, there is a notable quantitative difference between measured and predicted values that increases in magnitude with position y from the left to the right sample boundary and changes sign in between. One possible explanation for this discrepancy is that the constants f and g, which were fitted for a flat interface with a small misorientation angle, may depend on curvature. The fact that the sign of the difference between calculated and measured V_d values near each boundary depends on the sign of the macroscopic curvature, which has opposite signs for convex and concave interfaces, supports this interpretation. Solutal interactions of cells with the sample boundaries, which act as a source (left boundary) and sink (right boundary) of cells could further contribute to the difference between calculated and measured V_d values. However, the latter alone cannot easily explain how the sign of this difference changes with the sign of macroscopic curvature.

4.2.3 Pattern organization

We also perform a benchmark PF simulation in 3D to investigate the pattern organization observed in experiments at higher velocities ($V = 6$ and $12\ \mu\mathrm{m/s}$). Figure 13 shows the top view of a PF simulation with growth conditions $G = 12\ \mathrm{K/cm}$ and $V = 6\ \mu\mathrm{m/s}$, where the interface is macroscopically concave with a curvature amplitude $A = 284\ \mu\mathrm{m}$. Here we only focus on the range $0 \le y \le L/2$ from the left border to the sample center, i.e., $L_y = L/2$. The

wetting boundary condition is applied at $y = 0$ to represent the sample border, and the no-flux (symmetric) boundary condition is applied at $y = L_y$ to represent the sample center, where the local curvature is zero. The periodic boundary conditions are applied at $z = 0$ and $z = L_z$. The simulation domain size is $L_x \times L_y \times L_z = 900 \times 3900 \times 1160\ \mu m^3$, and the total simulated time is 4 h.

The initial condition is a disordered hexagonal array that was selected in a 3D PF simulation with a flat interface and no misorientation. We impose a misorientation angle $2.7°$ at $t = 0\ h$. As shown in Figure 13a at $t = 0.12\ h$, the disordered hexagonal array drifts to the right, and new dendrites are created at the source on the left border. Here, the dendritic array drifts in the $\langle 100 \rangle$ direction that is parallel to the preferred growth direction of secondary branches, and those secondary branches are normal to the simulation border. This simulation configuration can be compared to the experimental configuration of areas 1 to 4 of Figure 5, where the secondary branches are normal to the crucible border and the drifting velocity direction drives the pattern away from the border. The newly created dendrites form an aligned structure where dendrite primary trunks are aligned along the directions of the secondary branches. They progressively invade the disordered hexagonal array and form an invasion front (orange line) that shifts over time in the direction of the misorientation, as shown in Figures 13b-c. The aligned structure in the simulation is caused by the first type of source, i.e., the simulation boundary that represents a crucible border, and this observation qualitatively agrees with experimental observations in Figure 5.

5 Conclusion

In this paper, we have presented the analysis of a series of directional solidification experiments carried out in the DECLIC-DSI onboard the International Space Station on a transparent organic alloy (succinonitrile-0.46wt% camphor). Dendritic patterns' formation and evolution have been studied for a large range of pulling velocity. Changing this velocity strongly affects the furnace thermal field and the isotherms' shape so that macroscopic curvatures, i.e. curvatures of the envelope of the solidification front on a sample scale much larger than the dendritic array spacing, are obtained depending on the pulling velocity. Curvature naturally arises in a multitude of solidification processes from casting to additive manufacturing. Yet, the effect of curvature is largely unknown.

Our paper reports for the first time a quantitative study of the effect of the macroscopic curvature of the solidification front on the formation of dendritic microstructures, supported by both experiments and 3D phase-field simulations. Quantitative phase-field simulations with the implementation of curved isotherm shapes corresponding to the experiments were performed at experimental growth conditions. We demonstrated, both experimentally and numerically, that even a weak curvature can have a major effect on microstructure evolution and the striking results are summarized:

- A solid-liquid interface macroscopic curvature prevents the array from reaching a stationary state, which results in a primary spacing that does not stabilize: it increases continuously if the interface is convex and, inversely, decreases if the interface is concave.
- Dendrite stretching or reduction is caused by a radially symmetrical curvature-induced pattern drift (away from or towards this central region for a convex or concave interface,

respectively). This curvature-induced drift interacts with the unidirectional pattern drift induced by a small misorientation resulting in a macroscopic spatial gradient of drift velocity across the entire sample. Under the combined effect of curvature and misorientation, the spacing increases or decreases in the average drift direction induced by misorientation for a convex or concave interface, respectively.

- Interface concavity favors the stray grains propagation, which can even lead to the complete overgrowth of the well-oriented grain by off-axis grains. Overgrowth of the favorably oriented grain by off-axis subgrains of worse orientation appears to be generalized to all convergent boundaries in case of concavity. This generalization leads to a final grain texture formed by several off-axis grains.
- In the case of concavity, unusual arrangements of dendrites form along the directions of the secondary branches. These alignments result from the formation, due to drifting, of a periodic dendritic source by tertiary branching along the crucible border when secondary branches are roughly normal to the crucible border.

Experiments performed in the low gravity environment of space provided a unique opportunity to observe the formation and evolution of directionally solidified 3D extended dendritic patterns in diffusive transport conditions. The results presented here highlight the fundamental role of the macroscopic interface curvature on the characteristics and structuration of the pattern. Interface curvature is unavoidable in solidification processes and therefore it is important to be able to identify its effects. From this point of view, the results obtained here complement previous works elucidating the role of the complex and non-fixed thermal field in 3D configuration [30, 31], or of the influence of subgrains [32]. These characteristics, often dismissed as instrumental or experimental biases, are nevertheless critical in the real-world formation of solidification microstructures and must therefore be integrated in process relevant analyses and solidification models.

Acknowledgments

This work was supported by CNES (French Space Agency) and by NASA (National Aeronautics and Space Administration) Grants No. NNX12AK54G, 80NSSC19K0135, and 80NSSC22K0664. It is based on observations with the DECLIC-DSI (Directional Solidification Insert of the DEvice for the study of Critical LIquids and Crystallization) embarked on the ISS (International Space Station).

References

[1] M.C. Cross, P.C. Hohenberg, Pattern formation outside of equilibrium, Reviews of Modern Physics 65(3) (1993) 851-1112.
[2] J.D. Hunt, Solidification and casting of metals, london, 1979.
[3] W. Kurz, D.J. Fisher, Dendrite Growth at the Limit of Stability - Tip Radius and Spacing, Acta Metall. 29(1) (1981) 11-20.
[4] R. Trivedi, Interdendritic Spacing .2. A Comparison of Theory and Experiment, Metallurgical Transactions a-Physical Metallurgy and Materials Science 15(6) (1984) 977-982.

[5] S.H. Han, R. Trivedi, Primary Spacing Selection in Directionally Solidified Alloys, Acta Metallurgica Et Materialia 42(1) (1994) 25-41.
[6] K. Somboonsuk, J.T. Mason, R. Trivedi, Interdendritic Spacing .1. Experimental Studies, Metallurgical Transactions a-Physical Metallurgy and Materials Science 15(6) (1984) 967-975.
[7] K. Somboonsuk, R. Trivedi, Dynamical studies of dendritic growth, Acta Metall. 33(6) (1985) 1051-1060.
[8] R. Trivedi, K. Somboonsuk, Pattern-Formation during the Directional Solidification of Binary-Systems, Acta Metall. 33(6) (1985) 1061-1068.
[9] M.A. Eshelman, V. Seetharaman, R. Trivedi, Cellular spacings—I. Steady-state growth, Acta Metall. 36(4) (1988) 1165-1174.
[10] V. Seetharaman, M.A. Eshelman, R. Trivedi, Cellular spacings—II. Dynamical studies, Acta Metall. 36(4) (1988) 1175-1185.
[11] G. Hansen, S. Liu, S.Z. Lu, A. Hellawell, Dendritic array growth in the systems NH4Cl-H2O and [CH2CN](2)-H2O: steady state measurements and analysis, J. Cryst. Growth 234(4) (2002) 731-739.
[12] P. Mazumder, R. Trivedi, Integrated simulation of thermo-solutal convection and pattern formation in directional solidification, Applied Mathematical Modelling 28(1) (2004) 109-125.
[13] K.L. Scotti, L.G. Kearney, J. Burns, M. Ocana, L. Duros, A. Shelhamer, D.C. Dunand, The effect of solidification direction with respect to gravity on ice-templated TiO2 microstructures, Journal of the European Ceramic Society 39(10) (2019) 3180-3193.
[14] K.L. Scotti, E.E. Northard, A. Plunk, B.C. Tappan, D.C. Dunand, Directional solidification of aqueous TiO2 suspensions under reduced gravity, Acta Mater. 124 (2017) 608-619.
[15] M. Perrut, A. Parisi, S. Akamatsu, S. Bottin-Rousseau, G. Faivre, M. Plapp, Role of transverse temperature gradients in the generation of lamellar eutectic solidification patterns, Acta Mater. 58(5) (2010) 1761-1769.
[16] N. D'Souza, M.G. Ardakani, M. McLean, B.A. Shollock, Directional and single-crystal solidification of Ni-base superalloys: Part I. The role of curved isotherms on grain selection, MMTA 31(11) (2000) 2877-2886.
[17] K.A. Jackson, J.D. Hunt, Transparent compounds that freeze like metals, Acta Metall. 13(11) (1965) 1212-1215.
[18] C. Weiss, N. Bergeon, N. Mangelinck-Noel, B. Billia, Effects of the interface curvature on cellular and dendritic microstructures, Materials Science and Engineering a-Structural Materials Properties Microstructure and Processing 413 (2005) 296-301.
[19] H. Jamgotchian, N. Bergeon, D. Benielli, P. Voge, B. Billia, R. Guerin, Localized microstructures induced by fluid flow in directional solidification, Phys. Rev. Lett. 87(16) (2001) 166105.
[20] S. Bottin-Rousseau, A. Pocheau, Self-organized dynamics on a curved growth interface, Phys. Rev. Lett. 87(7) (2001) 6101.
[21] A. Pocheau, S. Bottin-Rousseau, Curvature induced periodic attractor on growth interface, Chaos 14(3) (2004) 882-902.
[22] B. Drevet, H. Nguyen Thi, D. Camel, B. Billia, M.D. Dupouy, Solidification of aluminium–lithium alloys near the cell/dendrite transition-influence of solutal convection, J. Cryst. Growth 218(2) (2000) 419-433.

[23] R. Trivedi, S. Liu, P. Mazumder, E. Simsek, Microstructure development in the directionally solidified Al-4.0 wt% Cu alloy system, Sci Technol Adv Mat 2(1) (2001) 309-320.
[24] F.L. Mota, Y. Song, J. Pereda, B. Billia, D. Tourret, J.-M. Debierre, R. Trivedi, A. Karma, N. Bergeon, Convection Effects During Bulk Transparent Alloy Solidification in DECLIC-DSI and Phase-Field Simulations in Diffusive Conditions, Jom 69(8) (2017) 1280-1288.
[25] V.T. Witusiewicz, L. Sturz, A. Viardin, C. Pickmann, G. Zimmermann, Effect of convection on directional solidification in transparent succinonitrile–2.2wt.%(d)camphor alloy, Acta Mater. 216 (2021) 117086.
[26] G. Reinhart, C.A. Gandin, N. Mangelinck-Noël, H. Nguyen-Thi, J.E. Spinelli, J. Baruchel, B. Billia, Influence of natural convection during upward directional solidification: A comparison between in situ X-ray radiography and direct simulation of the grain structure, Acta Mater. 61(13) (2013) 4765-4777.
[27] N. Bergeon, D. Tourret, L. Chen, J.-M. Debierre, R. Guerin, A. Ramirez, B. Billia, A. Karma, R. Trivedi, Spatiotemporal Dynamics of Oscillatory Cellular Patterns in Three-Dimensional Directional Solidification, Phys. Rev. Lett. 110(22) (2013).
[28] J. Pereda, F.L. Mota, L. Chen, B. Billia, D. Tourret, Y. Song, J.-M. Debierre, R. Guerin, A. Karma, R. Trivedi, N. Bergeon, Experimental observation of oscillatory cellular patterns in three-dimensional directional solidification, Phys. Rev. E 95(1) (2017) 012803.
[29] D. Tourret, J.-M. Debierre, Y. Song, F.L. Mota, N. Bergeon, R. Guerin, R. Trivedi, B. Billia, A. Karma, Oscillatory cellular patterns in three-dimensional directional solidification, Phys. Rev. E 92(4) (2015) 042401.
[30] F.L. Mota, N. Bergeon, D. Tourret, A. Karm, R. Trivedi, B. Billia, Initial transient behavior in directional solidification of a bulk transparent model alloy in a cylinder, Acta Mater. 85 (2015) 362-377.
[31] Y. Song, D. Tourret, F.L. Mota, J. Pereda, B. Billia, N. Bergeon, R. Trivedi, A. Karma, Thermal-field effects on interface dynamics and microstructure selection during alloy directional solidification, Acta Mater. 150 (2018) 139-152.
[32] F.L. Mota, J. Pereda, K. Ji, Y. Song, R. Trivedi, A. Karma, N. Bergeon, Effect of sub-boundaries on primary spacing dynamics during 3D directional solidification conducted on DECLIC-DSI, Acta Mater. 204 (2021).
[33] G. Pont, S. Barde, B. Zappoli, F. Duclos, Y. Garrabos, C. Lecoutre, D. Beysens, B. Billia, N. Bergeon, N. Mangelinck, R. Marcout, D. Blonde, DECLIC: a facility to study crystallization and critical fluids, 60th International Astronautical Congress, Daejeon, Republic of Korea, 2009.
[34] N. Bergeon, A. Ramirez, L. Chen, B. Billia, J. Gu, R. Trivedi, Dynamics of interface pattern formation in 3D alloy solidification: first results from experiments in the DECLIC directional solidification insert on the International Space Station, Journal of Materials Science 46(19) (2011) 6191-6202.
[35] J. Pereda, F.L. Mota, J.M. Debierre, B. Billia, R. Trivedi, A. Karma, N. Bergeon, Experimental characterization and theoretical analysis of cell tip oscillations in directional solidification, Phys. Rev. E 102(3) (2020) 032804.
[36] C. Weiss, N. Bergeon, N. Mangelinck-Noel, B. Billia, Cellular pattern dynamics on a concave interface in three-dimensional alloy solidification, Phys. Rev. E 79(1) (2009) 1605.
[37] See Supplementary Material at [URL will be inserted by publisher] for videos of experiments (thermal gradient = 12.5 K/cm ; Succinonitrile – 0.46 wt% Camphor): Video 1 _

Pulling rate = 1.5 µm/s ; Video 2 _ Pulling rate = 3 µm/s; Video 3 _ Pulling rate = 6 µm/s; Video 4 _ Pulling rate = 12 µm/s.
[38] J. Pereda, Y. Song, F.L. Mota, B. Billia, J.-M. Debierre, R. Guerin, A. Karma, R. Trivedi, N. Bergeon, Primary spacing evolution during microstructure formation in 3D directional solidification: methods of data treatment of microgravity experiments conducted in the DECLIC-DSI, 67th International Astronautical Congress, Guadalajara, Mexico, 2016.
[39] S. Akamatsu, T. Ihle, Similarity law for the tilt angle of dendrites in directional solidification of non-axially-oriented crystals, Phys. Rev. E 56(4) (1997) 4479-4485.
[40] J. Deschamps, M. Georgelin, A. Pocheau, Growth directions of microstructures in directional solidification of crystalline materials, Phys. Rev. E 78(1) (2008) 011605.
[41] J. Ghmadh, J.-M. Debierre, J. Deschamps, M. Georgelin, R. Guérin, A. Pocheau, Directional solidification of inclined structures in thin samples, Acta Mater. 74 (2014) 255-267.
[42] J. Deschamps, M. Georgelin, A. Pocheau, Growth directions of microstructures in directional solidification of crystalline materials, Phys. Rev. E 78(1) (2008) 1605.
[43] Y. Song, S. Akamatsu, S. Bottin-Rousseau, A. Karma, Propagative selection of tilted array patterns in directional solidification, Phys Rev Mater 2(5) (2018).
[44] D. Tourret, A. Karma, Growth competition of columnar dendritic grains: A phase-field study, Acta Mater. 82(0) (2015) 64-83.
[45] B. Billia, H. Jamgotchian, H.N. Thi, Statistical-Analysis of the Disorder of 2-Dimensional Cellular Arrays in Directional Solidification, Metallurgical Transactions a-Physical Metallurgy and Materials Science 22(12) (1991) 3041-3050.
[46] T. Takaki, S. Sakane, M. Ohno, Y. Shibuta, T. Shimokawabe, T. Aoki, Primary arm array during directional solidification of a single-crystal binary alloy: Large-scale phase-field study, Acta Mater. 118 (2016) 230-243.
[47] D. Walton, B. Chalmers, The origin of the preferred orientation in the columnar zone of ingots, Trans. AIME. 215 (1959) 447 - 457.
[48] N. D'Souza, M.G. Ardakani, A. Wagner, B.A. Shollock, M. McLean, Morphological aspects of competitive grain growth during directional solidification of a nickel-base superalloy, CMSX4, Journal of Materials Science 37(3) (2002) 481-487.
[49] A. Wagner, B.A. Shollock, M. McLean, Grain structure development in directional solidification of nickel-base superalloys, Materials Science and Engineering: A 374(1–2) (2004) 270-279.
[50] J. Li, Z. Wang, Y. Wang, J. Wang, Phase-field study of competitive dendritic growth of converging grains during directional solidification, Acta Mater. 60(4) (2012) 1478-1493.
[51] T. Takaki, M. Ohno, T. Shimokawabe, T. Aoki, Two-dimensional phase-field simulations of dendrite competitive growth during the directional solidification of a binary alloy bicrystal, Acta Mater. 81(0) (2014) 272-283.
[52] D. Tourret, Y. Song, A.J. Clarke, A. Karma, Grain growth competition during thin-sample directional solidification of dendritic microstructures: A phase-field study, Acta Mater. 122 (2017) 220-235.
[53] T. Takaki, S. Sakane, M. Ohno, Y. Shibuta, T. Aoki, Phase-field study on an array of tilted columnar dendrites during the directional solidification of a binary alloy, Computational Materials Science 203 (2022) 111143.
[54] J.A. Warren, J.S. Langer, Prediction of Dendritic Spacings in a Directional-Solidification Experiment, Phys. Rev. E 47(4) (1993) 2702-2712.

[55] J.D. Hunt, S.Z. Lu, Numerical modeling of cellular/dendritic array growth: spacing and structure predictions, MMTA 27(3) (1996) 611-623.
[56] G.L. Ding, W.D. Huang, X. Huang, X. Lin, Y.H. Zhou, On primary dendritic spacing during unidirectional solidification, Acta Mater. 44(9) (1996) 3705-3709.
[57] H. Chen, Y.S. Chen, X. Wu, S.N. Tewari, History dependence of primary dendrite spacing during directional solidification of binary metallic alloys and interdendritic convection, J. Cryst. Growth 253(1-4) (2003) 413-423.
[58] S. Gurevich, M. Amoorezaei, N. Provatas, Phase-field study of spacing evolution during transient growth, Phys. Rev. E 82(5) (2010).
[59] S. Gurevich, A. Karma, M. Plapp, R. Trivedi, Phase-field study of three-dimensional steady-state growth shapes in directional solidification, Phys. Rev. E 81(1) (2010) 1603.
[60] A. Karma, Phase-field formulation for quantitative modeling of alloy solidification, Phys. Rev. Lett. 87(11) (2001).
[61] B. Echebarria, R. Folch, A. Karma, M. Plapp, Quantitative phase-field model of alloy solidification, Phys. Rev. E 70(6) (2004) 061604.
[62] K.H. Ji, A.M. Tabrizi, A. Karma, Isotropic finite-difference approximations for phase-field simulations of polycrystalline alloy solidification, J. Comput. Phys. 457 (2022).
[63] F.L. Mota, L.M. Fabietti, N. Bergeon, L.L. Strutzenberg, A. Karma, B. Billia, R. Trivedi, Quantitative determination of the solidus line in the dilute limit of succinonitrile-camphor alloys, J. Cryst. Growth 447 (2016) 31-35.

Declaration of interests

☒ The authors declare that they have no known competing financial interests or personal relationships that could have appeared to influence the work reported in this paper.

☐The authors declare the following financial interests/personal relationships which may be considered as potential competing interests:

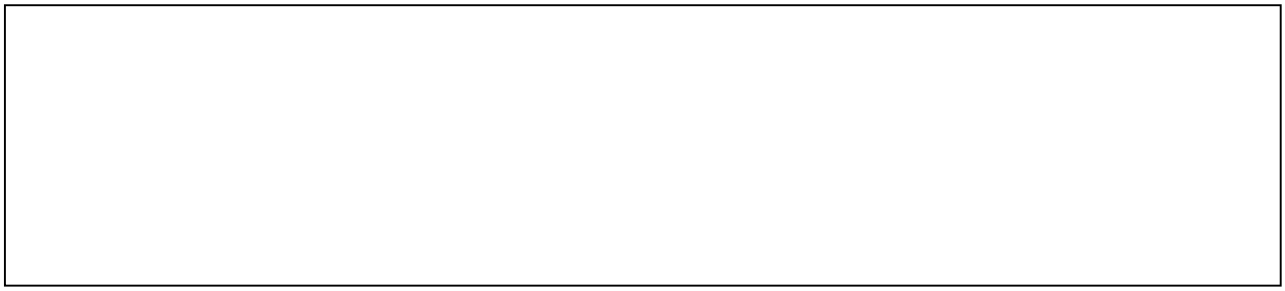

Graphical abstract

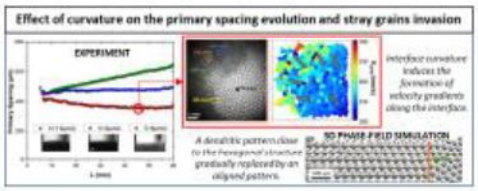

Figure 1. Sequence of formation of the interfacial microstructure (SCN–0.46 wt% camphor, V = 3 µm/s). Top images correspond to top-views of the interface, bottom images to the corresponding side views of the interface. t denotes the solidification time elapsed, and L the solidification length (L=Vt) attained. Video is provided in supplementary material (video2 of [37])

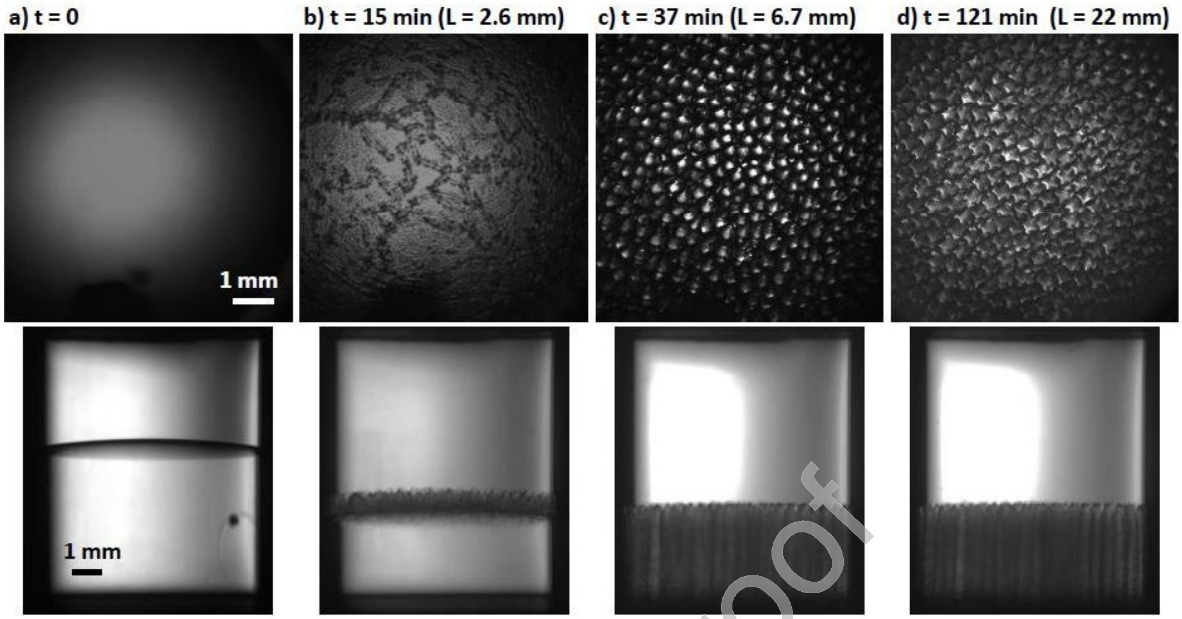

Figure 2. a) Top-view images of the interface for the different pulling velocities, V = 1.5, 3 , 6 and 12 µm/s, after pulling for respectively 8.3 h, 4.2 h, 2.1 h and 28 min. b) Maps of drift velocity (scale in nm/s) for the different pulling velocities for a grown length of 30 mm. The arrows represent the drift directions.

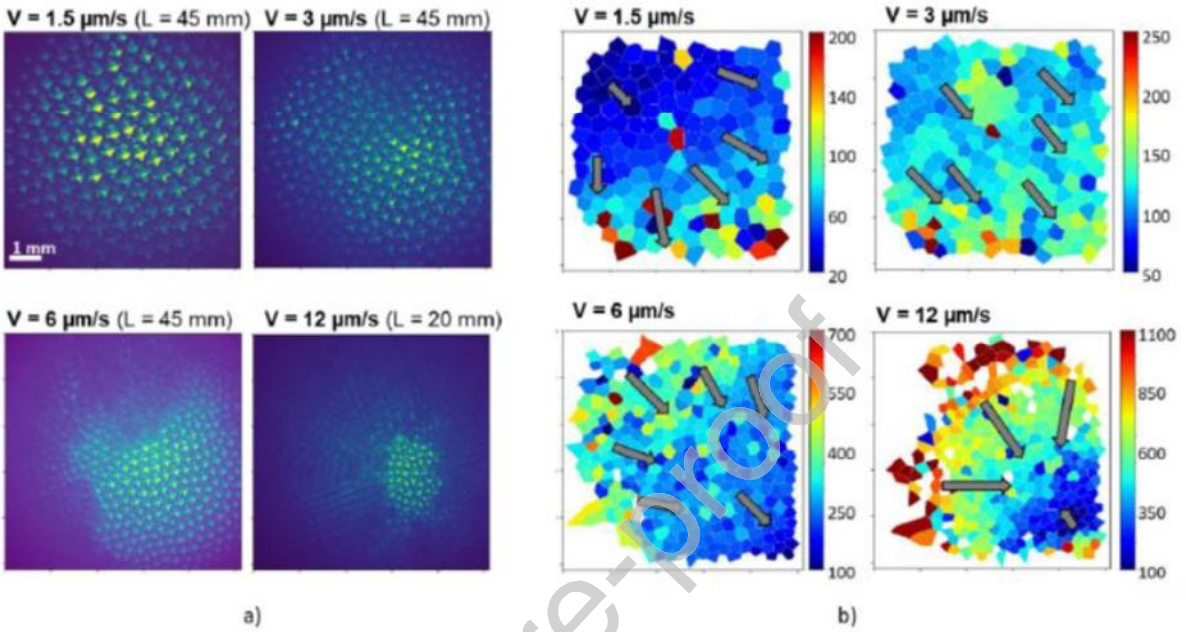

Figure 3. a) Experimental side-views of the solid-liquid interface and b) numerical calculations of the interface shape at rest and at steady-sate for the different pulling velocities.

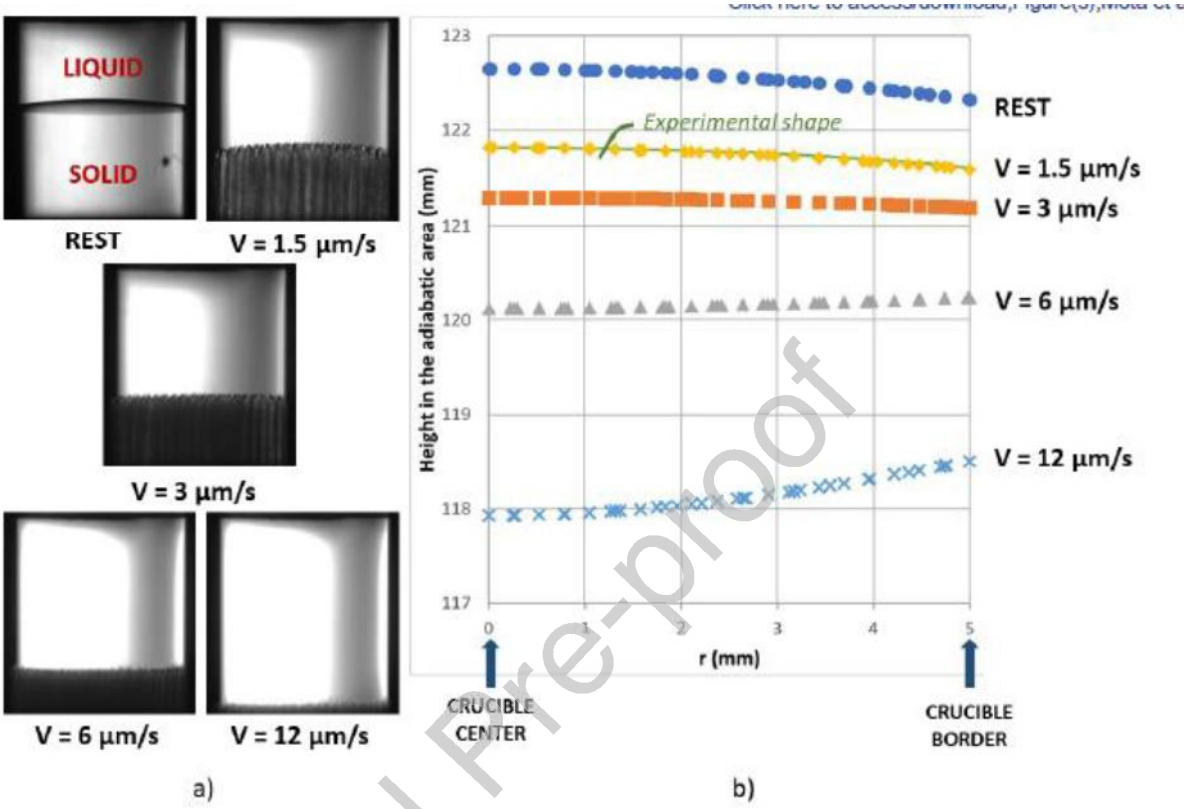

Figure 4. a) Scheme of the basic cases of drifting velocity for various local interface slope α. b) Occurrence of these basic cases along the interface for different types and amplitudes of curvature. Directions: $\overrightarrow{\boldsymbol{a}}$, orientation of the preferred <001>; $\vec{\boldsymbol{G}}$, thermal gradient; $\overrightarrow{\boldsymbol{V_I}}$, interface velocity; $\overrightarrow{\boldsymbol{V_g}}$, dendrite growth velocity; $\overrightarrow{\boldsymbol{V_d}}$, dendrite drift velocity. Angles: α, interface slope; θ_0 between $\overrightarrow{\boldsymbol{a}}$ and $\vec{\boldsymbol{G}}$; θ_g between $\overrightarrow{\boldsymbol{V_g}}$ and $\overrightarrow{\boldsymbol{V_I}}$; θ_{0_P} between $\vec{a}$ and $\overrightarrow{V_I}$ (equal to θ_0 for a local flat interface); θ between $\overrightarrow{\boldsymbol{a}}$ and $\overrightarrow{\boldsymbol{V_g}}$.

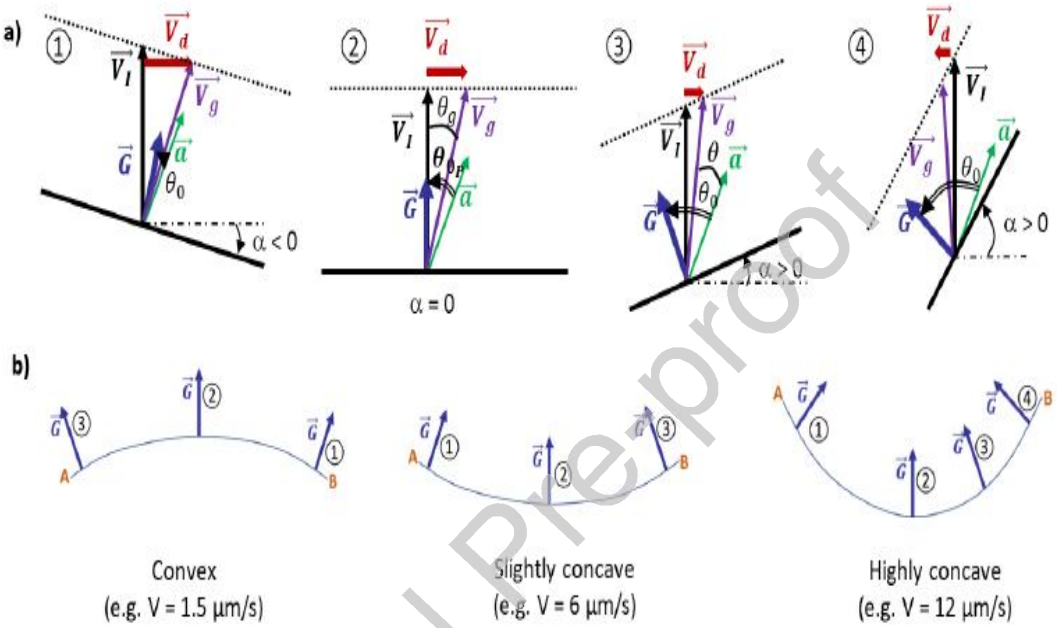

Figure 5. Study of invading sub-grains at V = a) 6 and b) 12 µm/s. Top view images of the interface after respectively 115 min and 61 min of growth. Rough limits of different stray-grains are drawn in a) to help visualization. For the different sub-grains, drifting velocity vectors of some dendrites are drawn and the corresponding module given. On b), stray-grains where dendrite tips are aligned with secondary branches appear : areas 1 to 4, enlarged in c). In areas 1 to 4, examples of alignments are given with markers positioned on dendrite tips. Such alignments are not observed in area 0 roughly located at 45° of secondary branches as illustrated on the scheme of d).

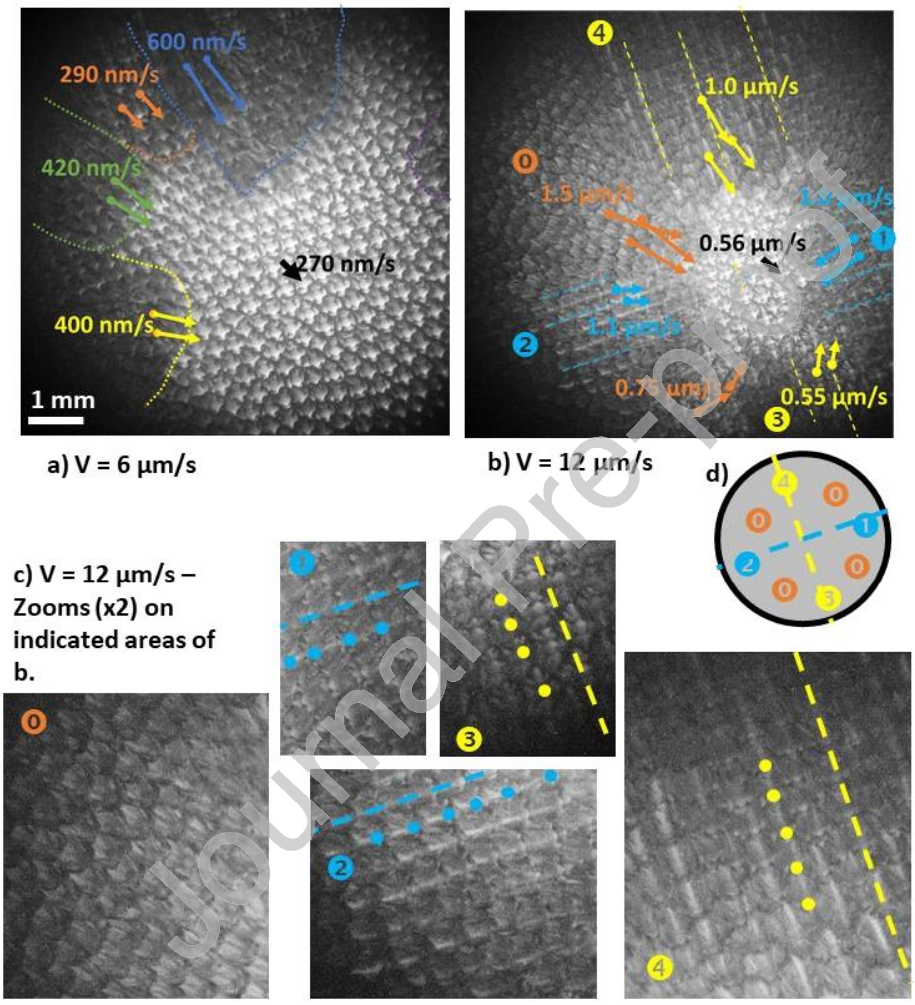

Figure 6. Time evolution of primary spacing for the different pulling velocities. In red : average values; maximum and minimum values are respectively in blue and yellow. For V = 1.5, 3 and 6 µm/s, measurements were performed during the whole solidification, starting just after the initial transient and ending after 60 mm of pulling. At V = 12 µm/s, measurements end after 36.8 mm of pulling with the disappearance of the well-oriented grain.

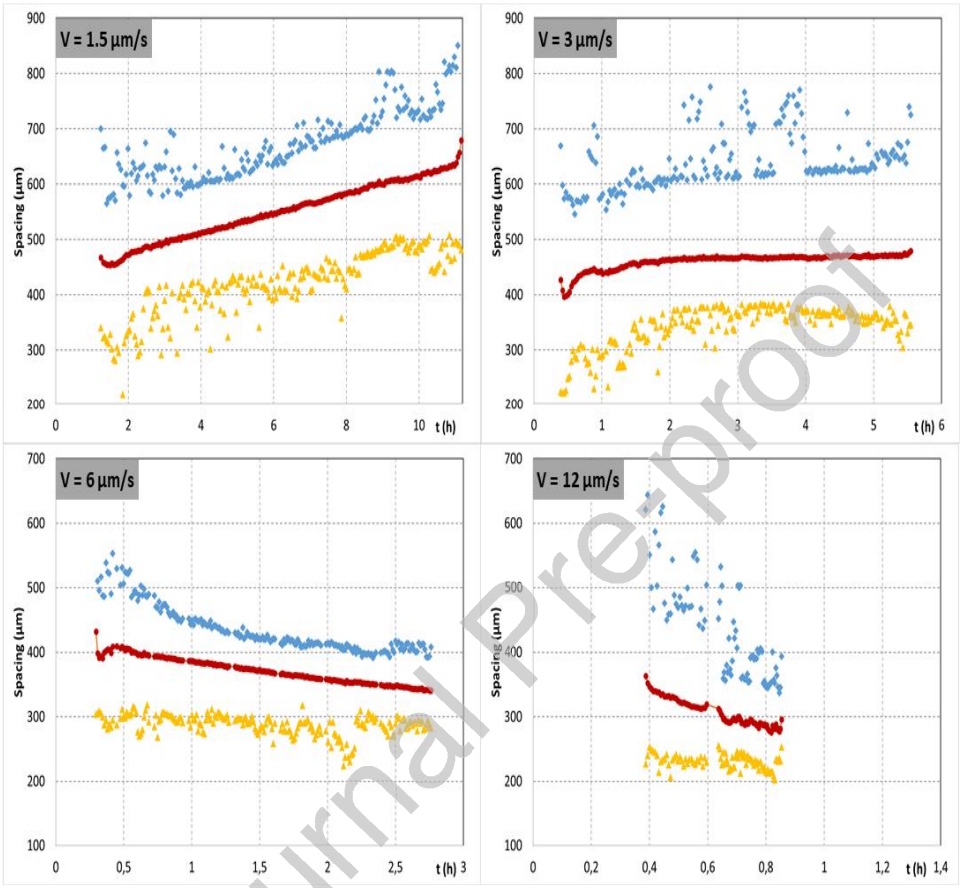

Figure 7. Spatial variation of primary spacing (b) and drifting velocity (c) for V = 1.5 µm/s. Measurements are performed in small regions defined in a). The evolution of spacing is characterized between 20 and 40 mm of pulling and compared to the local initial spacing for each area. The drifting velocity in each area is compared to the average value.

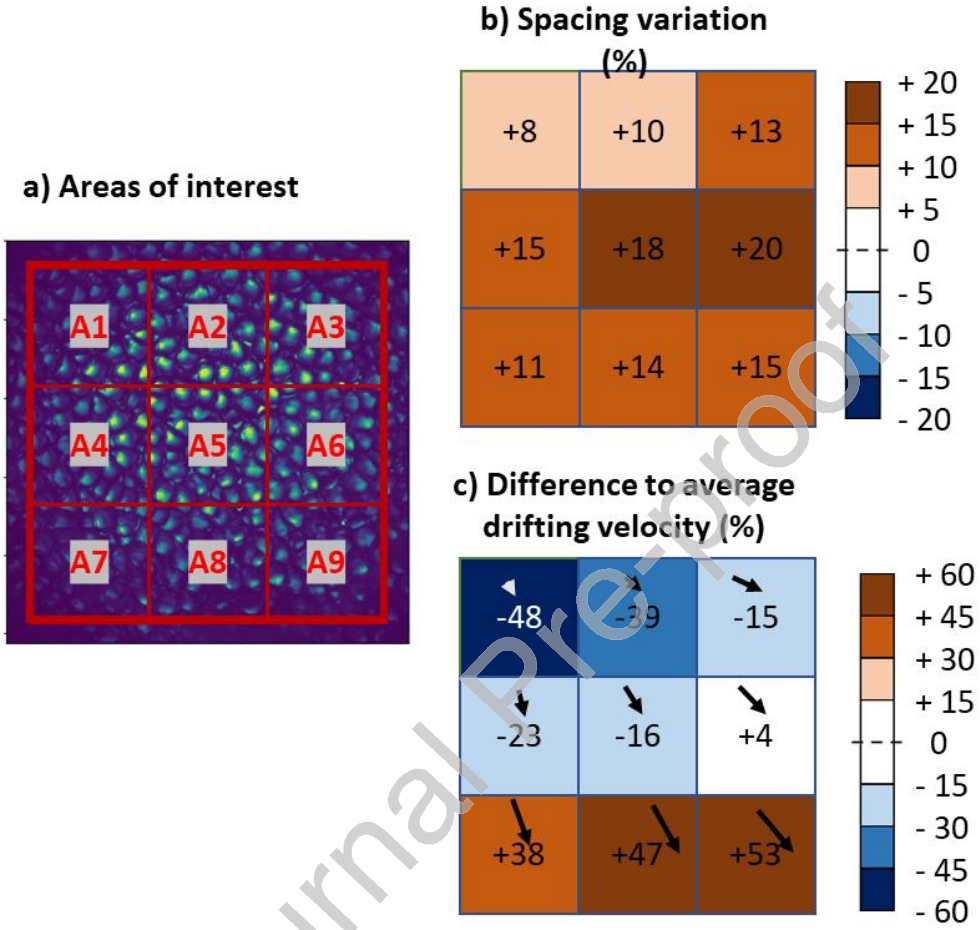

Figure 8. Scheme of building of the drifting velocity field for convex and concave interfaces. Misorientation induces a translational drift which is constant all along the interface (green arrows). Advection on a curved interface (blue arrows) is axisymmetric and its component increases when distancing from the center. The resulting drifting velocity is represented by the red arrows.

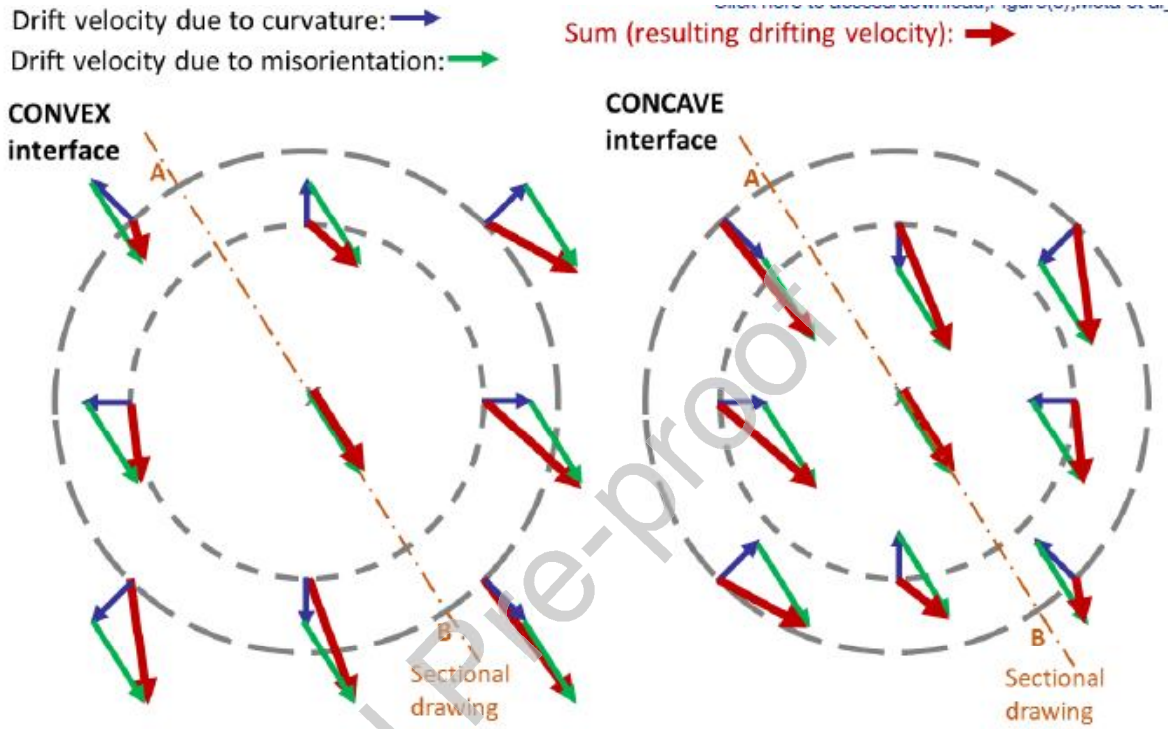

Figure 9. Analysis of drifting velocity profile along diagonal. All dendrites tagged in red are included in measurements for a) V = 1.5 and d) 6 µm/s. b) and e) Spatial primary spacing variation of the dendrites respectively tagged in a) and d). c) and f) Experimental and theoretically calculated profiles of the drifting velocity of the dendrites respectively tagged in a) and d). The r direction is schematically shown in a).

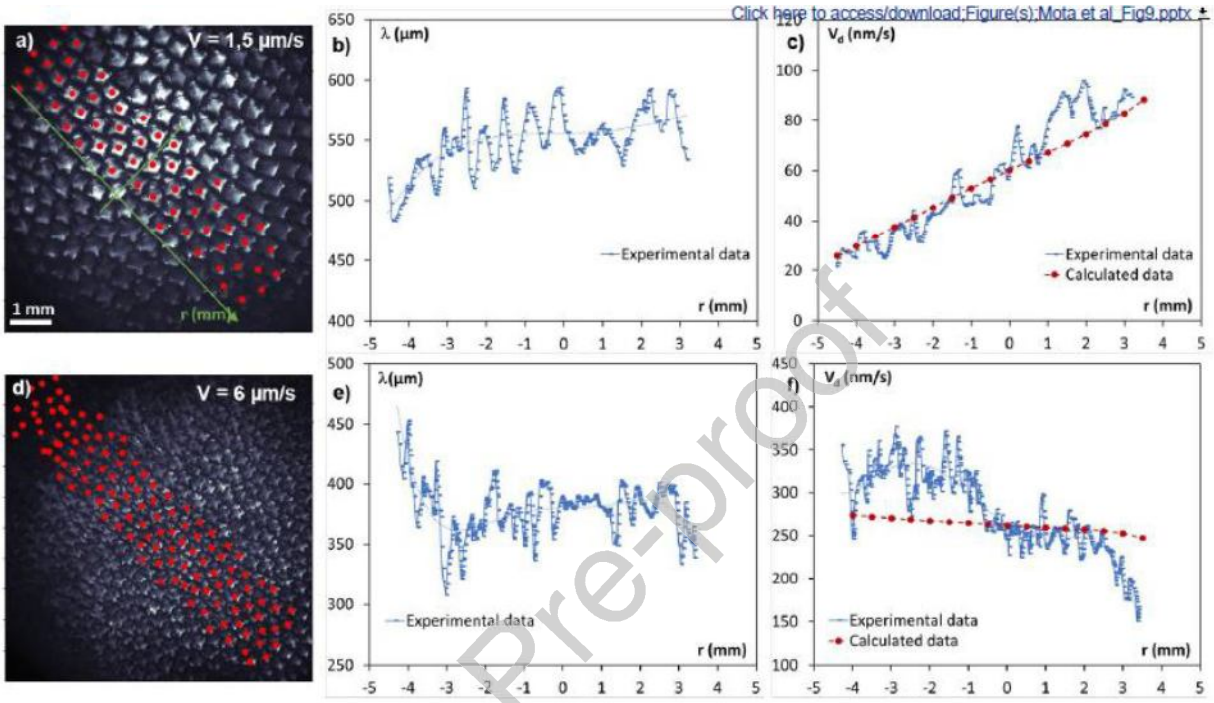

Figure 10. (a) Phase-field simulations of directional solidification of a SCN-0.46 wt% camphor alloy in a thin-sample geometry with a convex interface at V = 1.5 μm/s. (b) The evolution of the primary spacing λ in phase-field simulations of (a), where t_1 = 2.8, t_2 = 4.6, t_3 = 6.4, t_4 = 8.2, and t_5 = 10.0 h are the time after the beginning of the phase-field simulation from a planar interface. (c) Simulations with a concave interface at V = 6 μm/s. (d) The evolution of λ (c), where t_1 = 1.6, t_2 = 3.4, t_3 = 5.2, t_4 = 7.0, and t_5 = 8.8 h. The curves in (a) and (c) represent isotherms, and dots represent cell tips.

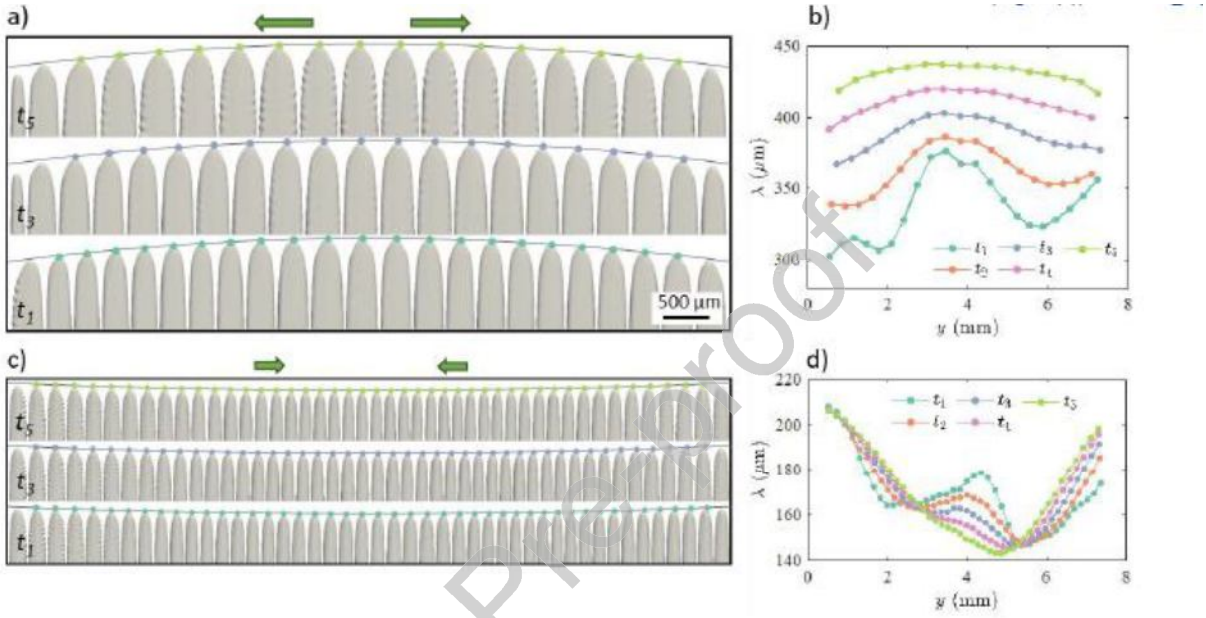

Figure 11. The evolution of the average primary spacing λ_{ave}, the maximum primary spacing λ_{max}, and the minimum primary spacing λ_{min} in phase-field simulations of directional solidification of an SCN-0.46 wt% camphor alloy in a thin-sample geometry with (a) a convex interface at $V = 1.5$ μm/s and (b) a concave interface at $V = 6$ μm/s.

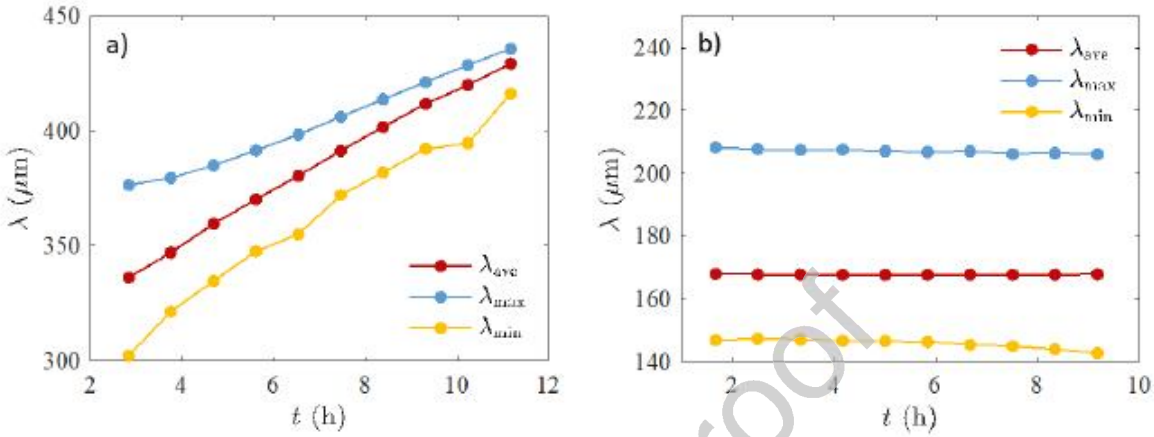

Figure 12. Analysis of drifting velocity profiles in phase-field simulations with an SCN-0.46 wt% camphor alloy performed for $G = 12$ K/cm, a) $V = 1.5$ μm/s, and b) $V = 6$ μm /s. The solid lines in blue represent the measured drifting velocity profiles, and the dashed lines in red represent the theoretically calculated drifting velocity profiles.

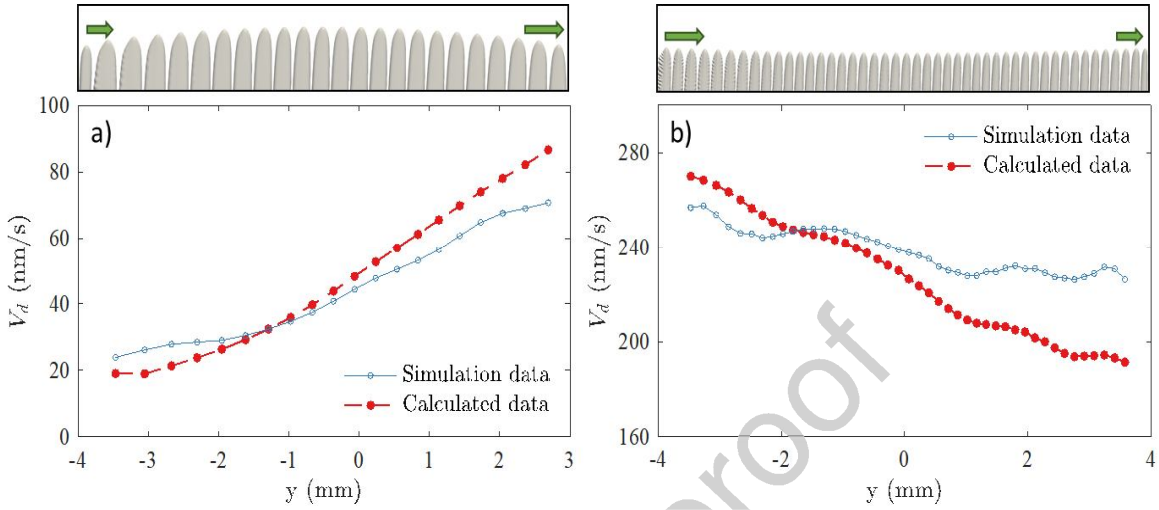

Figure 13. The invasion of dendrites formed at the left boundary (a source) in 3D phase-field simulations of directional solidification of an SCN-0.46 wt% camphor alloy with G = 12 K/cm and V = 6 μm/s, where the time t = (a) 0.12 h, (b) 2 h, and (c) 4 h. The interface is concave, and the misorientation angle is $\theta_0 = 2.7°$. A dendrite pattern close to the hexagonal structure is gradually replaced by an aligned pattern. The orange lines represent the invasion front.